# Ultrafast magnetization dynamics in an epitaxial $Ni_{54.3}Mn_{31.9}Sn_{13.8}$ Heusler-alloy film close to the Curie temperature

A. Bonda,[1,*] L. Uba,[1] K. Załęski,[2] and S. Uba[1]

[1]*Faculty of Mathematics and Informatics, University of Białystok, K. Ciołkowskiego 1M, 15-245 Białystok, Poland*

[2]*NanoBioMedical Centre, AMU, Wszechnicy Piastowskiej 3, 61-614 Poznań, Poland*

(Received 31 March 2019; published 17 May 2019)

The influence of the amplitude of an external magnetic field ($H$) and femtosecond laser pulse fluence ($F$) on ultrafast magnetization dynamics has been investigated in a ferromagnetic $Ni_{54.3}Mn_{31.9}Sn_{13.8}$ Heusler-alloy film using the time-resolved magneto-optical Kerr effect. A large slowing down of the demagnetization process was observed and characteristic parameters of magnetization precession were determined for a wide range of $H$ and $F$ values. Long demagnetization times of the order of hundreds of picoseconds have been found and explained as a result of the Curie temperature ($T_C$) proximity in the alloy film studied. Effective magnetic anisotropy field ($H_k^{eff}$) and Gilbert damping parameter dependencies were determined. A significant reduction of the precession frequency versus $F$ of the uniform Kittel mode was found. A strong decrease of $H_k^{eff}$ with $F$ was well simulated in the frame of an extended version of the microscopic three-temperature model (eM3TM), and explained by the $T_C$ proximity effect. The estimated low values of the eM3TM model parameters, the demagnetization rate and electron-lattice coupling constant, appeared essential to explain the slowing down effect of demagnetization. Precession amplitude dependencies were explained by a phenomenological approach taking into account $H_k^{eff}$ and changes of the equilibrium magnetization angles induced by pump-pulse excitation.

DOI: 10.1103/PhysRevB.99.184424

## I. INTRODUCTION

Advances in femtosecond laser spectroscopy opened the way toward developing the highest temporal resolution tool for studies of ultrafast magnetization dynamics [1,2]. It is a subject of intensive studies for both fundamental research importance [3] as well as applications in the field of ultrafast magnetic recording and spintronic devices [4–7]. An optical technique involving the time-resolved magneto-optical Kerr effect (TR-MOKE) significantly revised the view of demagnetization timescales and underlying mechanisms [8,9]. Ultrafast de- and remagnetization as well as magnetization precession processes have been investigated for a wide group of magnetic materials in a broad timescale range, from femtoseconds to nanoseconds [10–16]. Typically, demagnetization occurs within hundreds of fs for $3d$ transition metals [17–19] and tens of ps for $4f$ ferromagnets, while in the case of some half metals hundreds of ps were experimentally observed [20–22]. However, the mechanisms of ultrafast demagnetization, triggered by femtosecond optical laser pulses, are still under intensive debate and different types of spin-flip scattering and/or the spin-orbit interaction were considered as playing an important role in this process [23].

Most studies concerning different aspects of magnetization dynamics were performed as a function of an external magnetic field at temperatures far from the Curie temperature $T_C$ of the compounds [10,12,13,16,24–29]. The demagnetization critical slowing down effect was observed, e.g., in Gd [30], Ni [31,32], CoMnSb [11], and $CuCr_2Se_4$ [33] when the measurement temperature approaches $T_C$. A phenomenological description of the effect was proposed by Koopmans *et al.* in a microscopic three-temperature model (M3TM) [23]. Significant increases of the timescales of de- and remagnetization processes were also observed in half-metallic systems, e.g., $CrO_2$ [21] and $La_{0.6}Sr_{0.4}MnO_3$ [22,34]. However, the main mechanism in this case is related to temperature transfer channel blocking for the electron-spin interaction occurring after laser excitation [21,22].

Ultrafast magnetization precession phenomena are also an important subject of intense research and constitute different issues, due to the origin and different timescales ranging from tens of ps to several ns [12,25,35]. Both the magnetization precession frequencies and relaxation times have been investigated for various classes of materials in different experimental geometries and conditions (see, e.g., Refs. [15,33,36]). Different rates of the magnetization precession relaxation processes are observed, which are directly associated with the phenomenological Gilbert damping coefficient $\alpha$, related to energy dissipation in the magnetic system (see, e.g., Refs. [37,38]). The value of the $\alpha$ parameter determines the spin switching time, which is important from an application point of view [39–42].

Much attention in this field has been paid to Heusler alloys, since a group of them possesses a half-metallic nature and hence exhibits extremely low Gilbert damping [26,43,44] as a result of the suppression of spin-flip processes. Another interesting group is Ni-Mn-based Heusler alloys which belong to ferromagnetic shape-memory compounds and exhibit both ferromagnetic and structural transformations. They are smart functional materials with a wide range of possibilities for applications. They have attractive properties of the inverse

*a.bonda@uwb.edu.pl

 

magnetocaloric effect [45,46], a large magnetoresistance [46,47], and magnetic-field-induced strain [48,49]. The interest in ferromagnetic shape-memory compounds stems from the possibility of controlling the structural phase transition by magnetic fields [50]. A dynamical process of photoinduced martensitic transitions was recently studied in a Mn-rich, NiMnSn Heusler alloy [51,52]. However, studies of the ultrafast magnetization dynamics in this group of materials were performed, to our knowledge, only in the $Ni_2MnGa$ alloy in Refs. [53,54], and a preliminary study on the Ni-Mn-Sn alloy was undertaken in Ref. [55].

In this paper, we report a comprehensive study of the coherent spin precession dynamics in a Ni-Mn-Sn Heusler-alloy film using the TR-MOKE measurement technique. The motivation for this work was mainly to investigate ultrafast magnetization relaxation processes in an epitaxial $Ni_{54.3}Mn_{31.9}Sn_{13.8}$ alloy film, which exhibits $T_C$ about ≈20 K higher than room temperature. This additionally creates suitable conditions to observe the expected slowing down effect, not reported for both the Ni-Mn-based but also for other Heusler alloys [11].

The aim of the work is twofold: the systematic study of (i) the de- and remagnetization effects and (ii) the magnetization precession processes—both in timescales from a few of ps to ns, performed as a function of an external magnetic field and pump-pulse fluence. The dependencies of the magnetization precession frequencies, relaxation times, damping parameters, amplitudes, and effective magnetic anisotropy fields were determined. The slowing down effect of demagnetization was observed for a wide range of magnetic fields and fluences, and explained in the frame of an extended microscopic three-temperature model (eM3TM) which takes into account a medium thermal reservoir. Magnetization precession amplitude dependencies versus the magnetic field and fluence have been determined and explained in the frame of a phenomenological model which takes into account the effective magnetic anisotropy field ($H_k^{\rm eff}$) and changes of the equilibrium magnetization angles induced by pump pulses. A strong reduction of $H_k^{\rm eff}$ with an increase of fluence has been observed, and was quantitatively explained using the eM3TM model as a result of the $T_C$ proximity effect in the Heusler-alloy film studied.

The paper is organized as follows. In Sec. II, the experimental conditions for TR-MOKE measurements and other experimental details are described. In Sec. III, theoretical aspects concerning the Landau-Lifshitz-Gilbert equation, the results of measurements and data analysis, and an interpretation of the results in the frame of the phenomenological approach and eM3TM model are presented. A summary and conclusions are included in Sec. IV.

## II. EXPERIMENTAL DETAILS

The time-resolved magneto-optical Kerr effect has been measured for Ni- and Mn-rich Ni-Mn-Sn shape-memory alloy film of $Ni_{54.3}Mn_{31.9}Sn_{13.8}$ composition at an ambient temperature $T_a = 297$ K, which is much higher than the martensitic phase transition temperature $T_M = 115$ K measured in this alloy [56].

The method of preparation and characterization of the sample is described in Refs. [56,57]. The 100-nm-thick epitaxial Ni-Mn-Sn alloy film was prepared by the magnetron sputtering method. The film was deposited at 500 °C on a single-crystalline MgO(001) substrate. The chemical composition of the sample was determined from an x-ray fluorescence analysis [56,57]. From x-ray diffraction measurements the epitaxial relationship of the film was confirmed to be Ni-Mn-Sn[100]/MgO(001)[110]. The Curie temperature of the $Ni_{54.3}Mn_{31.9}Sn_{13.8}$ film $T_C = 319$ K was determined from a direct measurement of magnetization as a function of temperature.

The ultrafast magnetization dynamics of the Ni-Mn-Sn alloy film was studied using the TR-MOKE method in combination with the standard dual color pump-probe technique. In the experimental setup, a Ti:sapphire regenerative amplifier system (Spitfire Ace, Spectra-Physics) nominally generating ∼35-fs pulses at a 10-kHz repetition rate was used. The pump pulses induce the magnetization dynamics processes at a laser fundamental wavelength of 800 nm, while the time-delayed probe pulses were frequency doubled by a beta barium borate (BBO) crystal and detected at 400 nm. The measurements were performed within a long-range, up to 3.5 ns, time window with a resolution of about 1 ps. Both pump and probe beams of $s$ polarization were focused on the sample at angles of incidence of ∼5° and ∼25°, respectively. It has been checked that the change in pump beam polarization does not affect the general character of the recorded signal, as it was observed already in the case of transition metals [58–60]. To avoid the inhomogeneity of the excited film area, the pump beam was focused to ∼240 $\mu$m, while the probe spot diameter was about three times smaller. Transient Kerr rotation was synchronously detected using a balanced optical bridge detector.

The magnetization dynamics in the $Ni_{54.3}Mn_{31.9}Sn_{13.8}$ alloy film was examined using TR-MOKE measurements performed as a function of (1) the amplitude of the external magnetic field $H$ generated by the electromagnet and (2) the fluence $F$ of the pumping pulses. The first scenario was implemented for varying $H$ amplitude, up to 6 kOe, under a constant fluence 0.35 mJ/cm$^2$. In the second scenario, $H$ was fixed at 1.5 kOe and the excitation-pump fluence $F$ was varied in the range of 0.07–0.9 mJ/cm$^2$. In both cases, $H$ was applied at an angle $\theta_H \approx 45°$ with respect to the sample normal. Other experimental setup details are similar as in Refs. [55,61]. The optical parameters for the film studied were determined from spectral ellipsometry measurements, and for $\lambda = 800$, the refractive index $n = 2.352$, extinction coefficient $k = 3.117$, and reflectivity $R = 0.55$. Static MOKE measurements were performed using a magneto-optical magnetometer setup based on the light polarization modulation technique [62].

## III. EXPERIMENTAL RESULTS, COMPARISON WITH THEORETICAL MODEL, AND DISCUSSION

### A. Precession of magnetization

The uniform magnetization precession is described by the Landau-Lifshitz-Gilbert (LLG) equation [63–65]

$$(1+\alpha^2)\frac{d\mathbf{M}(t)}{dt} = -\gamma_0[\mathbf{M}(t)\times\mathbf{H}^{\rm eff}(t)] - \frac{\alpha\gamma_0}{M_s} \times\{\mathbf{M}(t)\times[\mathbf{M}(t)\times\mathbf{H}^{\rm eff}(t)]\}, \quad (1)$$

where $\mathbf{M}(t)$ is the magnetization given as a function of delay time $t$, $\mathbf{H}^{\text{eff}} = \mathbf{H} + \mathbf{H}_{\text{k}}^{\text{eff}}$ is the effective field acting on the magnetization, $\mathbf{H}$ is the external magnetic field, and $\mathbf{H}_{\text{k}}^{\text{eff}}$ is the effective magnetic anisotropy field of the sample.

Time-independent quantities in Eq. (1) are the Gilbert damping coefficient $\alpha$, saturation magnetization $M_{\text{s}}$, and gyromagnetic ratio $\gamma_0 = \frac{g\mu_B}{\hbar}$, where $g$ is the gyromagnetic splitting factor $g = 2.0023$ for free electrons.

The solution of Eq. (1) describes the precession of the magnetization vector $\mathbf{M}(t)$ around $\mathbf{H}^{\text{eff}}$. The incoming pump laser pulse temporarily changes the $\mathbf{H}_{\text{k}}^{\text{eff}}$ and forces the magnetization to undergo a precession. For a given value of external field $H$, applied at an angle $\theta_H$ with respect to the sample normal, the precession frequency $f$ is expressed by

$$f(H, \theta_H) = \frac{\gamma}{2\pi}\sqrt{H_1 H_2}, \tag{2}$$

where

$$H_1 = H\cos(\theta_H - \theta) + H_{\text{k}}^{\text{eff}}\cos^2\theta,$$
$$H_2 = H\cos(\theta_H - \theta) + H_{\text{k}}^{\text{eff}}\cos 2\theta,$$

and $\gamma = \gamma_0/(1+\alpha^2)$ [64–67]. The angle $\theta$ defines the direction of magnetization $\mathbf{M}(t)$ with respect to the sample normal and fulfills the equilibrium equation

$$\sin 2\theta = \frac{2H}{H_{\text{k}}^{\text{eff}}}\sin(\theta_H - \theta). \tag{3}$$

The relaxation time $\tau$ of the magnetization precession is related to the $\alpha$ parameter through the equation [68]

$$1/\tau = \frac{\alpha\gamma(H_1 + H_2)}{2(1+\alpha^2)}. \tag{4}$$

It should be noted that, when values of $f$ and $\tau$ quantities are known, the solution of Eqs. (2)–(4) allows one to determine the $\alpha$, $H_{\text{k}}^{\text{eff}}$, and $\theta$ parameters. During the precession, the changes of the $\mathbf{M}(t)$ components over time are detected in the reflection geometry as the transient Kerr rotation $\Delta\theta_{\text{K}}(t)$ in the TR-MOKE experiment. It is convenient to express the measured TR-MOKE versus delay time $t$ between the pump and probe pulse as a sum of two components given by the formula

$$\Delta\theta_{\text{K}}(t) = A\exp\left(-\frac{t}{\tau}\right)\sin(2\pi f t + \varphi) + B(t), \tag{5}$$

where $A$, $f$, $\varphi$, and $\tau$ are the amplitude, frequency, phase, and relaxation time of the magnetization precession, respectively. The first component, denoted hereafter as $\Delta\theta_{\text{K}}^{\text{osc}}(t)$, represents the damped oscillatory function describing the decay of magnetization precession, and $B(t)$ represents a nonoscillating background, related to the sample demagnetization and recovery processes.

### B. Experimental results and data analysis

The $\Delta\theta_{\text{K}}(t)$ dependencies in the $Ni_{54.3}Mn_{31.9}Sn_{13.8}$ alloy film measured for different magnetic fields $H$ at a fixed pump fluence $F = 0.35$ mJ/cm$^2$ are shown in Fig. 1(a). For each value of $H$, the $\Delta\theta_{\text{K}}(t)$ dependencies consist of a damped oscillating component on a slowly changing in time nonoscillating background. It is clearly seen that the frequency of the

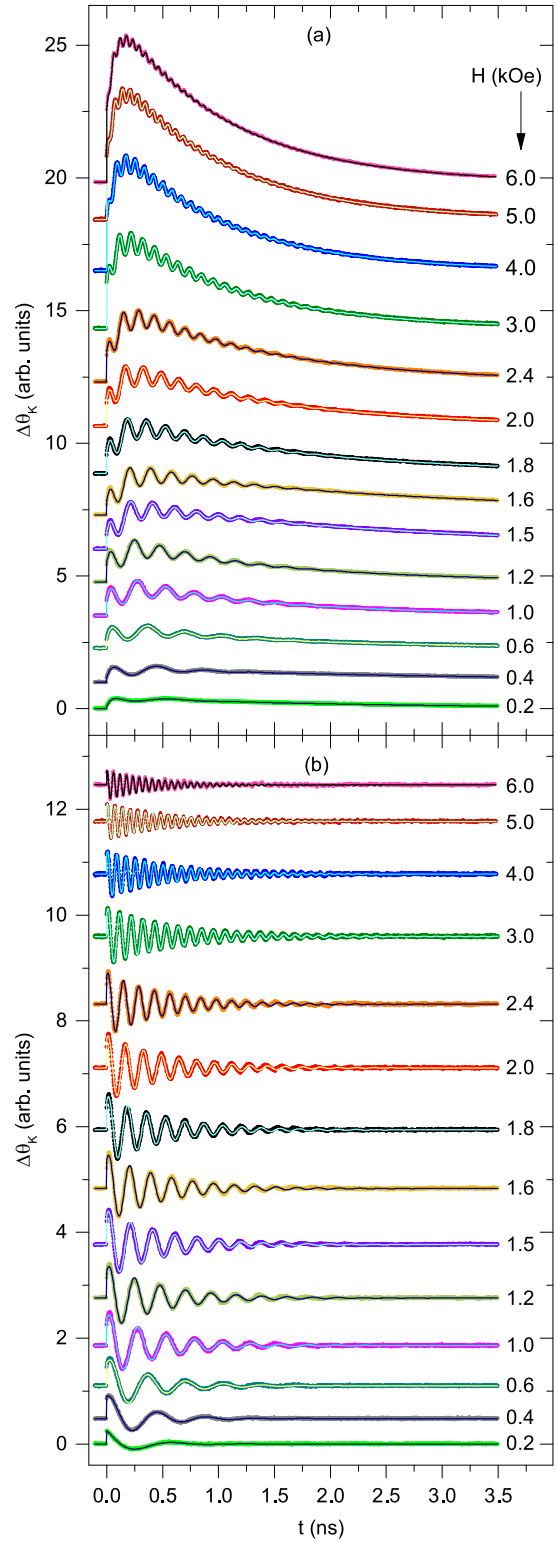


FIG. 1. Transient Kerr rotation measurements (circles) at different magnetic field $H$ values in $Ni_{54.3}Mn_{31.9}Sn_{13.8}$ and their best fits according to Eq. (5) (lines) at a constant pump-pulse fluence $F = 0.35$ mJ/cm$^2$. The total measured TR-MOKE dependencies with corresponding fits are shown in (a). The oscillatory components, with subtracted backgrounds in accord with Eqs. (6a)–(6c), are shown in (b). The curves are vertically shifted for clarity.

oscillating component increases with an increase of $H$, while the amplitude of the oscillations decreases. Temporal $\Delta\theta_K(t)$ dependencies measured for different fluences $F$ at fixed $H = 1.5$ kOe are shown in Fig. 2(a). The overall features of $\Delta\theta_K(t)$ are similar to those in the previous case, but a distinct decrease of the precession frequency with increasing $F$ is clearly seen. In both scenarios studied, a strong increase of $\Delta\theta_K(t)$ magnitude with $H$ and $F$ is observed [see Figs. 1(a) and 2(a)]. It should be noted that the above presented general character of a slow signal buildup versus delay time is rarely observed, and is similar to the one reported for $La_{1.2}Sr_{1.8}Mn_2O_7$ [69] and for MnAlGe [70], but on a much shorter timescale in the latter case.

To study the influence of $H$ and $F$ on $\Delta\theta_K^{osc}(t)$ quantitatively, the decomposition of the measured $\Delta\theta_K(t)$ on the oscillating $\Delta\theta_K^{osc}(t)$ and nonoscillating $B(t)$ contributions should be performed. A correct procedure requires a relevant modeling of the $B(t)$ function. A rough inspection of the measured $\Delta\theta_K(t)$ dependencies in Figs. 1(a) and 2(a) suggests that the biexponential form of the $B(t)$ function as a sum of fast $B_f(t)$ and slow $B_s(t)$ terms,

$$B(t) = B_f(t) + B_s(t), \tag{6a}$$

$$B_f(t) = B_f^0 \exp\left(-\frac{t}{\tau_f}\right), \tag{6b}$$

$$B_s(t) = B_s^0 \exp\left(-\frac{t}{\tau_s}\right), \tag{6c}$$

should be assumed. In Eqs. (6a)–(6c), $B_f^0$ and $B_s^0$ are amplitudes, and $\tau_f$ and $\tau_s$ are fast and slow relaxation times, respectively.

For all measured $\Delta\theta_K(t)$ dependencies, the fitting procedure according to Eq. (5) with $B(t)$ given by Eqs. (6a)–(6c) was performed. The fitted curves are shown in Figs. 1(a) and 2(a) by solid lines. Very good agreement between measured and fitted dependencies confirms the correctness of the adopted $B(t)$ function. The typical $B(t)$, $B_f(t)$, and $B_s(t)$ functions, obtained in the fitting procedure for $\Delta\theta_K(t)$ measured at $H = 1.5$ kOe and $F = 0.35$ mJ/cm$^2$, are shown in Fig. 3. It is seen that the $B_f(t)$ and $B_s(t)$ terms have comparable amplitudes and differ significantly in the relaxation time values $\tau_f = 107$ ps and $\tau_s = 1.56$ ns, respectively. Modeling of $B(t)$ in the frame of the extended version of the microscopic three-temperature model will be presented in Sec. III C.

Hereafter, we will focus on the oscillatory $\Delta\theta_K^{osc}(t)$ component related to magnetization precession. The $\Delta\theta_K^{osc}(t)$ has been determined by subtracting the fitted $B(t)$ background from the measured $\Delta\theta_K(t)$. The procedure was applied to all experimental data shown in Figs. 1(a) and 2(a). Oscillatory $\Delta\theta_K^{osc}(t)$ dependencies with a gradually changing precession frequency $f$, amplitude $A$, and relaxation time $\tau$ with increasing $H$ and $F$ are shown in Figs. 1(b) and 2(b), respectively. The fitted $\Delta\theta_K^{osc}(t)$ functions are marked by solid lines in Figs. 1(b) and 2(b).

The dependencies of the $f$, $\tau$, and $A$ parameters versus $H$ and $F$, obtained in the fitting procedure according to Eq. (5), are shown in Figs. 4(a)–4(c) and 5(a)–5(c), respectively. The $f(H)$ dependence [see Fig. 4(a)] is typical for the magnetization precession frequency related to the Kittel mode.

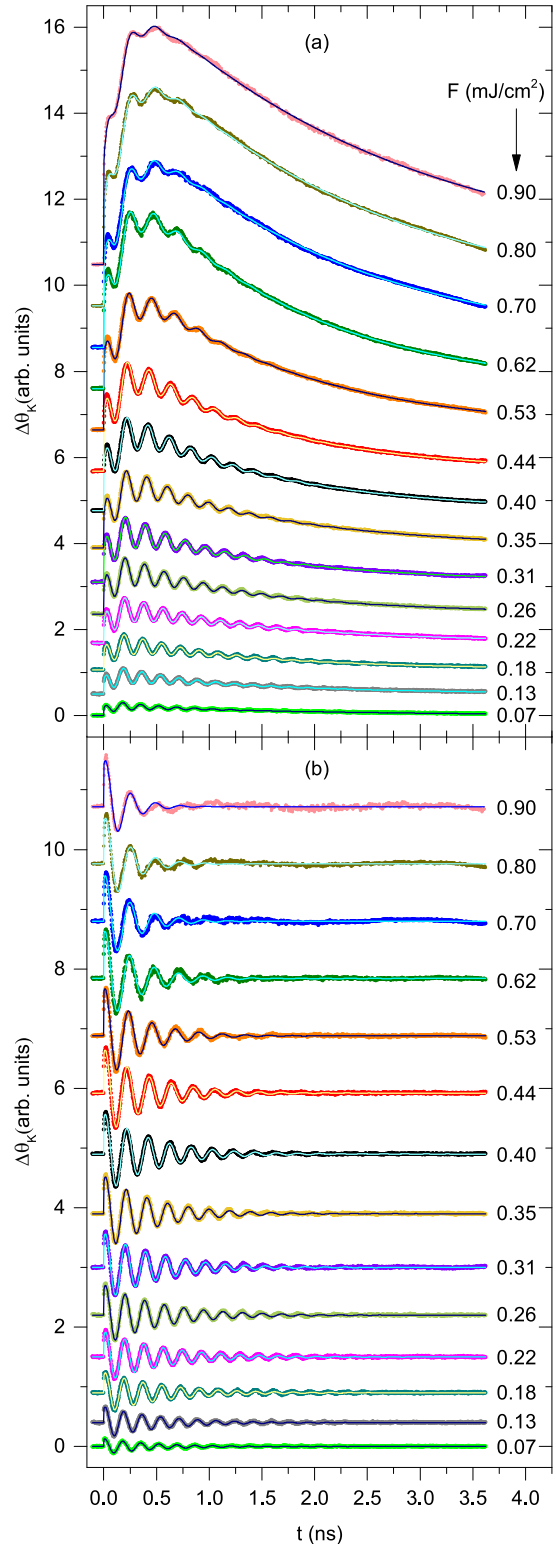


FIG. 2. Transient Kerr rotation measurements (circles) at different pump-pulse fluences $F$ in $Ni_{54.3}Mn_{31.9}Sn_{13.8}$ and their best fits according to Eq. 5 (lines) at a constant magnetic field $H = 1.5$ kOe. The total measured TR-MOKE dependencies with corresponding fits are shown in (a). The oscillatory components, with subtracted backgrounds in accord with Eqs. (6a)–(6c), are shown in (b). The curves are vertically shifted for clarity.

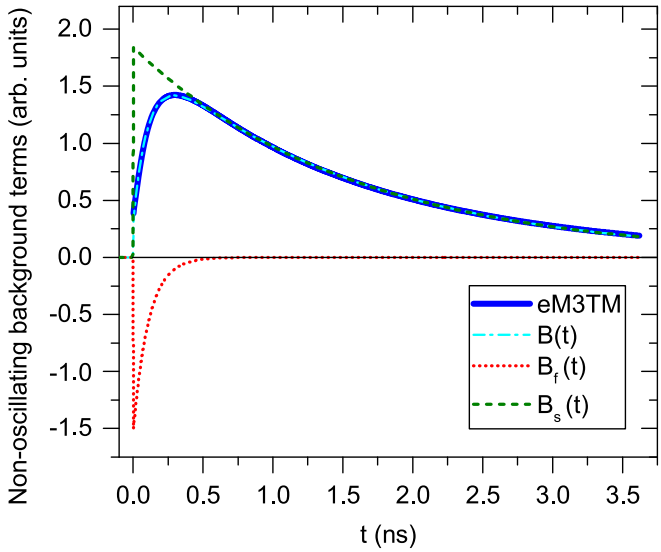


FIG. 3. Nonoscillating background $B(t)$ decomposition (dashed-dotted sea-blue line) on the fast $B_f(t)$ (dotted red line) and slow $B_s(t)$ (dashed green line) contributions of TR-MOKE dependence measured for $H = 1.5$ kOe and $F = 0.35$ mJ/cm$^2$. The thick blue line represents the demagnetization $\Delta m(t)$ function obtained within the eM3TM model (see Sec. III C for details).

The $f(H)$ increases linearly for $H \gtrsim 1$ kOe, and reaches a value of 16 GHz at $H = 6$ kOe. The relaxation time $\tau(H)$ [see Fig. 4(b)] shows a sharp decrease in the range $H =$ 0.05–0.15 kOe and then increases to a maximum value of 0.5 ns. The precession amplitude $A(H)$, shown in Fig. 4(c), increases with $H$ reaching the maximum value at $H \approx 1.8$ kOe and then significantly decreases for higher fields.

The dependencies of $f(F)$, $\tau(F)$, and $A(F)$ parameters on the laser pulse fluence $F$ at a constant field $H = 1.5$ kOe are shown in Figs. 5(a)–5(c). It should be noted that the precession frequency $f(F)$ is not constant but decreases considerably from 5.9 GHz at $F = 0.07$ mJ/cm$^2$ to 4.1 GHz at $F = 0.9$ mJ/cm$^2$. The rate of the $f(F)$ change decreases for $F \gtrsim 0.6$ mJ/cm$^2$. The relaxation time $\tau(F)$, shown in Fig. 5(b), has a maximum value of ≈0.6 ns at $F \approx 0.22$ mJ/cm$^2$, and then decreases monotonically with $F$ reaching a value of about 0.25 ns at $F \approx 0.9$ mJ/cm$^2$. The precession amplitude $A(F)$, shown in Fig. 5(c), increases initially with $F$, saturates at $F \approx 0.53$ mJ/cm$^2$, and then decreases.

### *1. Determination of Gilbert damping and effective magnetic anisotropy field parameters*

The $\alpha$, $H_k^{\text{eff}}$, and $\theta$ dependencies on $H$ and $F$ were determined solving Eqs. (2)–(4) by using as input data the $f$ and $\tau$ values obtained previously in the fitting procedure. The damping parameter $\alpha$, together with the effective damping $\alpha_{\text{eff}}$, calculated accordingly to the formula $\alpha_{\text{eff}} = 1/(2\pi f \tau)$, is shown in Fig. 4(d). Both $\alpha_{\text{eff}}(H)$ and $\alpha(H)$ exhibit sharp maxima at around $H = 0.1$ kOe with the magnitude equal to ≈0.55 and ≈0.2, respectively [see Fig. 4(d)]. This behavior originates from the presence of a domain structure in the

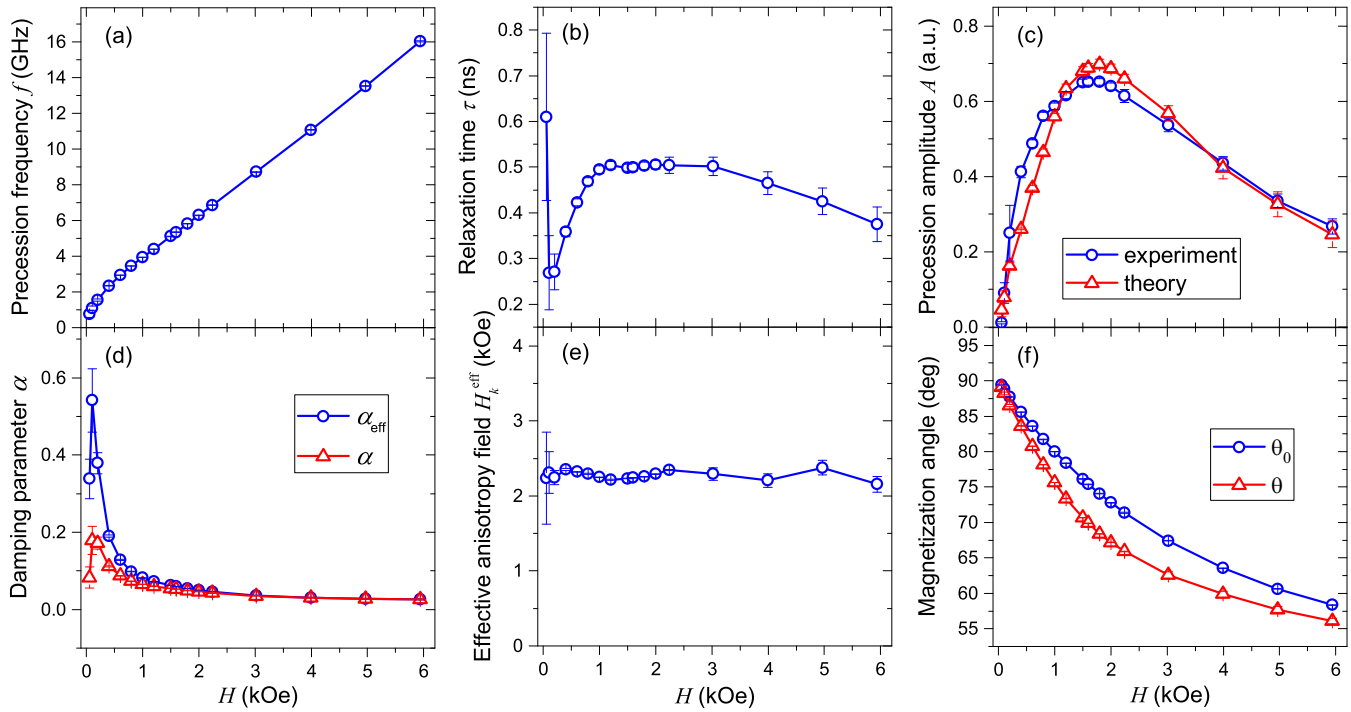


FIG. 4. Dependence of magnetization precession parameters on the magnetic field $H$ at fluence $F = 0.35$ mJ/cm$^2$. (a) Precession frequency $f$, (b) relaxation time $\tau$, (c) amplitude $A$ (blue circles), and (d) effective damping parameter $\alpha_{\text{eff}}$ (blue circles) are obtained from a fitting of Eq. (5) to the transient Kerr rotation in Fig. 1. (d) Gilbert damping parameter $\alpha$ (red triangles), (e) effective magnetic anisotropy field $H_k^{\text{eff}}$, and (f) magnetization angles $\theta_0$ (blue circles) and $\theta$ (red triangles), are obtained from the solution of Eqs. (2)–(4). (c) Simulated precession amplitude (red triangles) is calculated using Eq. (8).

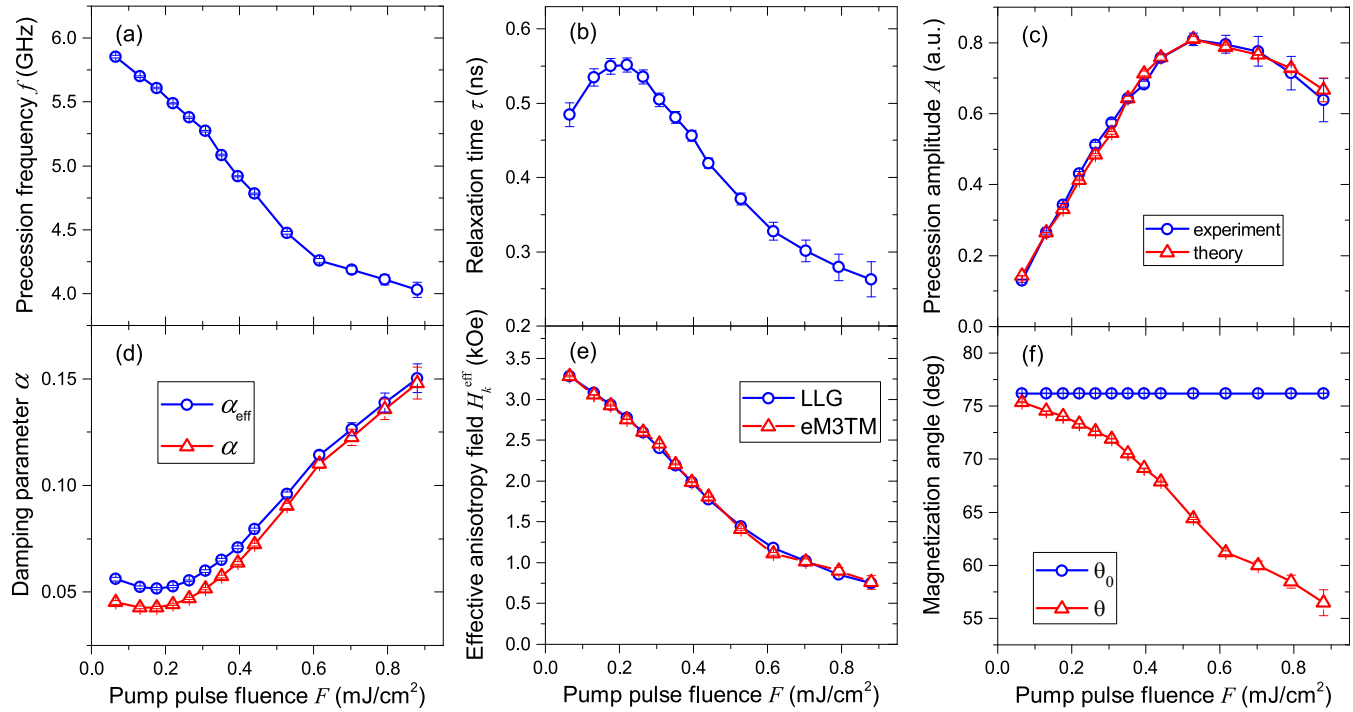


FIG. 5. Dependence of magnetization precession parameters on the pulse fluence $F$ at magnetic field $H = 1.5$ kOe. (a) Precession frequency $f$, (b) relaxation time $\tau$, (c) amplitude $A$ (blue circles), and (d) effective damping parameter $\alpha_{\text{eff}}$ (blue circles) are obtained from the fitting of Eq. (5) to the transient Kerr rotation in Fig. 1. (d) Gilbert damping parameter $\alpha$ (red triangles), (e) effective magnetic anisotropy field $H_{\text{k}}^{\text{eff}}$, and (f) magnetization angles $\theta_0$ (blue circles) and $\theta$ (red triangles), are obtained from the solution of Eqs. (2)–(4). (c) The simulated precession amplitude (red triangles) is calculated using Eq. (8). The simulated $H_{\text{k}}^{\text{eff}}(F)$ dependence obtained from the solution of the eM3TM model is shown in (e) by the red triangles (see Sec. III C).

$Ni_{54.3}Mn_{31.9}Sn_{13.8}$ alloy film studied which persists up to $H \approx 0.07$ kOe [see Fig. 1(b) in Ref. [71]]. It should be noted that $\alpha_{\text{eff}}(H)$ is significantly larger as compared to $\alpha(H)$ at low fields. In high fields, $\alpha_{\text{eff}}(H)$ asymptotically approaches $\alpha(H)$ dependence with $\alpha = 0.026$ at $H = 6$ kOe. This behavior follows from the asymptotical relation $\alpha_{\text{eff}} = \alpha/(1+\alpha^2)$ that can be derived from Eqs. (2)–(4) in the high-field limit. The lower value of the $\alpha = 0.009$ parameter as determined in the ferromagnetic resonance (FMR) experiment for a stoichiometric $Ni_{50}Mn_{25}Sn_{25}$ Heusler-alloy film [57] can result from a slightly different composition and also from the transient heating effect which can contribute to the enhancement of $\alpha$ in the case of the TR-MOKE experiment [72].

The calculated effective magnetic anisotropy field $H_{\text{k}}^{\text{eff}}(H)$ is shown in Fig. 4(e). As expected, $H_{\text{k}}^{\text{eff}}$ does not depend on $H$ to within experimental fluctuations (the weighted average of $H_{\text{k}}^{\text{eff}} \approx 2.26$ kOe, with a standard deviation of 0.03 kOe).

The solutions of Eqs. (2)–(4) for different pump-pulse fluences at a constant magnetic field $H = 1.5$ kOe are shown in Figs. 5(d) and 5(e). Both $\alpha(F)$ and $\alpha_{\text{eff}}(F)$, shown in Fig. 5(d), depend weakly on $F$ up to $F \approx 0.3$ mJ/cm$^2$ and increase over three times at $F \approx 0.9$ mJ/cm$^2$. In contrast to the case of field dependencies of damping parameters, the differences between the $\alpha(F)$ and $\alpha_{\text{eff}}(F)$ functions are small. This behavior follows from the high value of $H = 1.5$ kOe in the case considered [see Fig. 4(d)].

The dependence of $H_{\text{k}}^{\text{eff}}(F)$ is shown in Fig. 5(e). It shows a strong, nearly linear decrease of $H_{\text{k}}^{\text{eff}}$ down to ≈1.1 kOe with the fluence increasing up to $F \approx 0.6$ mJ/cm$^2$, however, a less pronounced slope of the dependence can be observed for $F$ in the range of 0.6–0.9 mJ/cm$^2$.

To qualitatively explain the $H_{\text{k}}^{\text{eff}}(F)$ dependence in the alloy film studied, we will make an assumption that in the vicinity of $T_{\text{C}}$ the main contribution to $H_{\text{k}}^{\text{eff}}$ originates from the shape anisotropy $H_{\text{d}} = 4\pi M$. The dependence of $M(t)$ in the temperature range from $T_{\text{a}}$ to $T_{\text{C}}$ for the film studied can be approximated by the mean-field formula $M(t) \propto (T - T_{\text{C}})^{\beta}$ with a critical exponent $\beta = 0.5$. This value is very close to that for a bulk $Ni_{50}Mn_{35}Sn_{15}$ alloy ($\beta = 0.456$ in Ref. [73] and $\beta = 0.501$ in Ref. [74]). From the mean-field formula, the dependence $T(F)$, related to the increase of the effective temperature that is induced in the sample by laser pulses, can be expressed as

$$T(F) = T_{\text{C}} - \left[h_{\text{k}}^{\text{eff}}(F)\right]^{(1/\beta)}(T_{\text{C}} - T_{\text{a}}), \tag{7}$$

where $h_{\text{k}}^{\text{eff}}(F) = H_{\text{k}}^{\text{eff}}(F)/H_{\text{k}}^{\text{eff}}(F \to 0)$. Using $T_{\text{C}}$ and $T_{\text{a}}$ values (see Sec. II), $H_{\text{k}}^{\text{eff}}(F)$ from Fig. 5(e), and $H_{\text{k}}^{\text{eff}}(F \to 0) = 3.52$ kOe [determined from the extrapolation of the $H_{\text{k}}^{\text{eff}}(F)$ function to $F = 0$], the $T(F)$ dependence can be calculated. The result is shown in Fig. 6. It shows an approximately linear increase of $T(F)$, which saturates at $F \approx 0.6$ mJ/cm$^2$. For this fluence, the effective temperature reaches a value of 318 K. This temperature differs from the Curie temperature by only 1 K, however, $H_{\text{k}}^{\text{eff}}$ still has a considerable value of 0.7 kOe [see Fig. 5(e)]. This aspect will be discussed in Sec. III C.

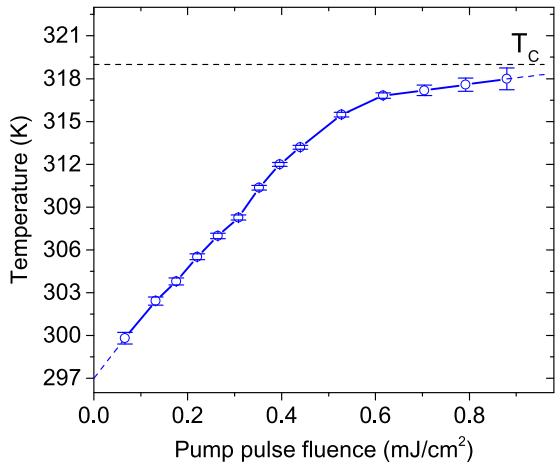


FIG. 6. Effective temperature in the $Ni_{54.3}Mn_{31.9}Sn_{13.8}$ alloy film, calculated as a function of pulse fluence $F$ with the use of Eq. (7).

#### 2. *Amplitude of magnetization precession*

In order to accurately describe the magnetization precession amplitude $A$ vs $H$ and $F$, the differential LLG equation (1) should be numerically solved (see, e.g., Refs. [70,75–77]). In an approximate approach, $A$ can be simulated qualitatively with an analytical formula derived under the assumption that the cone angle of the precession is sufficiently small, and hence using the differentiation of the magnetization equilibrium equation (3) (see, e.g., Ref. [77]). However, it appears that for the film studied, the precession cone angle $\Delta\theta = \theta_0 - \theta$ (where $\theta_0$ and $\theta$ are magnetization direction equilibrium angles before and after laser pulse excitation, respectively) is significant. The $\theta(H)$, shown in Fig. 4(f), was calculated from Eq. (3) for $H_k^{\rm eff} = 2.26$ kOe, while $\theta_0(H)$ was derived for $H_k^{\rm eff}(F \to 0) = 3.52$ kOe, taken from the $H_k^{\rm eff}(F)$ dependence shown in Fig. 5(e). Both angles monotonically decrease with $H$, which corresponds to the magnetization direction change from the sample plane ($\theta = \theta_0 = 90^\circ$ for $H = 0$) towards the direction of the magnetic field applied at $\theta_H = 45^\circ$. It should be noted that after the initial increase, the difference $\Delta\theta = \theta_0 - \theta$ saturates at around $H \approx 1.8$ kOe and then decreases for higher fields. In the following, the amplitude of the transient Kerr rotation will be expressed as

$$A \propto H_k^{\rm eff} \sin(\Delta\theta)\sin(\theta). \tag{8}$$

In Eq. (8), the factor $\sin(\theta)$ relates to the projection of the precession trajectory of the **M** vector on the $z$ axis, which corresponds to the polar component of the transient Kerr rotation. The precession amplitude $A(H)$ was calculated from Eq. (8) using $\theta_0(H)$ and $\theta(H)$ from Fig. 4(f), and is shown in Fig. 4(c). The $A(H)$ describes well the amplitude determined previously using Eq. (5). The decrease of the $A(H)$ at high fields can be easily understood from the fact that with increasing $H$, both the equilibrium magnetization angles $\theta_0(H)$ and $\theta(H)$ asymptotically approach the applied field angle $\theta_H$, and $\Delta\theta$ as well as $A(H)$ tends to zero.

The magnetization precession amplitude $A$ vs $F$ was determined using the above described procedure. The magnetization angle $\theta_0 = 76^\circ$ at $H = 1.5$ kOe was taken from the data in Fig. 4(f). The $\theta_0$ and $\theta(F)$, calculated using Eq. (3), are shown in Fig. 5(f). The fast decrease of the magnetization angle from $\theta_0 \approx 76^\circ$ down to $\theta \approx 56^\circ$ is a direct consequence of the strong decrease of $H_k^{\rm eff}$ with $F$. The precession amplitude $A(F)$ calculated with the use of Eq. (8) [shown in Fig. 5(c) by the red triangles] coincides very well, to within error bars, with the amplitude $A$ determined directly from the $\Delta\theta_K^{\rm osc}(t)$ dependencies. $A(F)$ increases nearly linearly with the fluence up to around $F = 0.4$ mJ/cm$^2$, due to the increase of $\Delta\theta(F)$ with $F$. However, $A(F)$ saturates at $F \approx 0.5$ mJ/cm$^2$, and then decreases for $F$ in the range 0.6–0.9 mJ/cm$^2$. The saturation behavior of $A(F)$ with an increase of the fluence can be understood by considering the interplay between the $H_k^{\rm eff}(F)$ and $\Delta\theta(F)$ dependencies. The decrease of $A(F)$ for $F \gtrsim 0.5$ mJ/cm$^2$ is related to the faster decrease of $H_k^{\rm eff}(F)$ as compared to the $\Delta\theta(F)$ increase.

### C. Extended microscopic three-temperature model

An attempt to understand the origin of the phenomena, observed in the TR-MOKE experiment in the $Ni_{54.3}Mn_{31.9}Sn_{13.8}$ alloy film, has been undertaken using the thermodynamical approach. As a basis, the microscopic three-temperature model developed by Koopmans *et al.* in Ref. [23] was adopted. The model was extended by including an additional medium thermal reservoir with a constant temperature $T_a$ considered as a thermostat [78,79]. In the extended model, in addition to terms describing the electronic and lattice thermal reservoirs, the term representing the cooling process of the lattice with a relaxation time $\tau_a$ to the ambient temperature $T_a$ is introduced. We used the following set of differential equations,

$$\frac{dT_e}{dt} = \frac{(T_l - T_e)}{\tau_{le}} + \frac{P(t)}{C_e}, \tag{9a}$$

$$\frac{dT_l}{dt} = \frac{(T_e - T_l)}{\tau_{el}} + \frac{(T_a - T_l)}{\tau_a}, \tag{9b}$$

$$\frac{dm}{dt} = R\,m\frac{T_l}{T_C}\left[1 - m\coth\left(m\frac{T_C}{T_e}\right)\right], \tag{9c}$$

$$\frac{dT_a}{dt} = 0, \tag{9d}$$

where $m = M/M_s$ is the relative magnetization, $T_e$ and $T_l$ are the electronic and lattice subsystem temperatures, and $\tau_{le} = C_e/g_{el}$ and $\tau_{el} = C_l/g_{el}$ are corresponding relaxation times. $C_e = \gamma_e T_e$ and $C_l$ are the electronic and lattice thermal capacities, respectively, and $g_{le} = g_{el}$ is the thermal electron-lattice coupling constant. $P(t)$ represents the energy introduced into the system by the ultrafast laser pulses. The temporal function $P(t)$ depends on laser pulse parameters such as fluence and pulse duration, and on material specific parameters such as sample absorptivity and light penetration depth. Equation (9c) describes the temporal dependence of the relative magnetization $m(t)$, where $T_C$ is the Curie temperature of the material and $R$ is the prefactor controlling the demagnetization rate [23,80].

We numerically solved Eqs. (9a)–(9d) using the values of the parameters as follows. For $C_l$, we took the value $3.443 \times 10^6$ J m$^{-3}$ K$^{-1}$, averaged from the values for similar composition alloys, $Ni_{50}Mn_{35}Sn_{15}$ [81] and $Ni_{50}Mn_{34}Sn_{16}$

[82], and for $\gamma_e$ the value of 386 J m$^{-3}$ K$^{-2}$ [81] was assumed. The $P(t)$ Gaussian temporal function was calculated for the material specific and laser pulse parameters listed in Sec. II. The values of the parameters $\tau_a$, $g_{el}$, and $R$ were fitted with the use of a scaling factor in the procedure based on a comparison of the relative demagnetization, defined as $\Delta m(t) = m(0) - m(t)$, obtained from the solution of Eqs. (9a)–(9d), with $B(t)$ derived from the measured $\Delta\theta_K(t)$. The $\Delta m(t)$ dependence fitted to $B(t)$ is shown by the thick blue line in Fig. 3. It is seen that the $\Delta m(t)$ function reproduces very well the $B(t)$ dependence.

In the following, we will discuss the fitted parameter values of the eM3TM model. The $\tau_{le}$ and $\tau_{el}$ relaxation times were estimated to be 0.5 ps and 14.5, respectively. Comparing these times with the much larger $\tau_f = 107$ ps time determined in Sec. III B, it can be argued that neither $\tau_{le}$ nor $\tau_{el}$ but $\tau_f$ can be considered as the value characterizing the slow demagnetization time. This value is up to two orders of magnitude larger as compared to demagnetization times reported for common ferromagnetic materials [10,17–19]. It is also much larger as compared to the CoMnSb Heusler alloy, where a relatively long demagnetization time of 18 ps was ascribed as a result of the low $T_C = 474$ K, which leads to a thermally induced slowing down of the demagnetization [11].

As to the fitted $\tau_a = 1.67$ ns parameter of the eM3TM model, it should be noted that this value is very close to the value of $\tau_s = 1.56$ ns, estimated in Sec. III B for the $B_s(t)$ background. This is due to the fact that the asymptotic solution of Eqs. (9a)–(9d) for a cooling process is described by an exponentially decaying function in the long time limit.

It should be stated that the observed demagnetization slowing down effect is related to the extremely low values of $g_{el} = 0.24 \times 10^{18}$ J m$^{-3}$ s$^{-1}$K$^{-1}$ and $R = 0.10 \times 10^{12}$ s$^{-1}$ fitted model parameters. These values are over an order of magnitude smaller than those in Ni; however, both parameters are close to those determined for Gd [23].

In Ref. [83], Kimling *et al.* studied the demagnetization behavior in the $Fe_{46}Cu_6Pt_{48}$ layer at different temperatures under a low laser fluence. They found that the slowing down of ultrafast demagnetization is dominated by a significant increase of the magnetic heat capacity $C_s$ near $T_C$ in this system. Therefore, the question arises about the accuracy of the approximation used in the eM3TM model in which the $C_s$ component has been neglected. In order to take into account $C_s$ in the eM3TM model, the total heat capacity $C_t = C_l + C_s(t)$ should be considered, instead of a constant $C_l$ value. Thus, the temperature and time-dependent $C_s(t)$ should be used in Eqs. (9a)–(9d). In the case of the $Ni_{50}Mn_{35}Sn_{15}$ alloy, the contribution of $C_s$ to $C_t$ is about 25% at $T_C$ [81], in contrast to the ≈50% contribution for $Fe_{46}Cu_6Pt_{48}$ (see Ref. [83]). We estimated the upper limit for the changes of the $g_{el}$ and $R$ parameters assuming for $C_s$ the value at $T_C$ taken from Ref. [81]. With this modification the resulting value of the $g_{el}$ parameter increased by about 16%, while $R$ decreased by about 8%. Thus, it can be stated that accounting for the magnetic heat capacity in the eM3TM model does not change the general conclusions about the low values of the $g_{el}$ and $R$ parameters for the $Ni_{54.3}Mn_{31.9}Sn_{13.8}$ alloy film studied.

As discussed in Ref. [23], one of the reasons for the low value of $R$ can be related to the strong reduction of the minority-spin density of states (DOS). Using linear-muffin-tin-orbital (LMTO) *ab initio* methods, we performed spin-polarized band-structure calculations for the austenite phase of an off-stoichiometric alloy of $Ni_{53.2}Mn_{31.3}Sn_{15.6}$ composition, close to the alloy studied. The total and partial density of states for Ni and Mn sites are shown in Fig. 7. As can be seen, the total DOS for the minority electronic band is about two times larger than that for the majority one, and cannot be considered to be responsible for the low value of $R$ in the alloy studied.

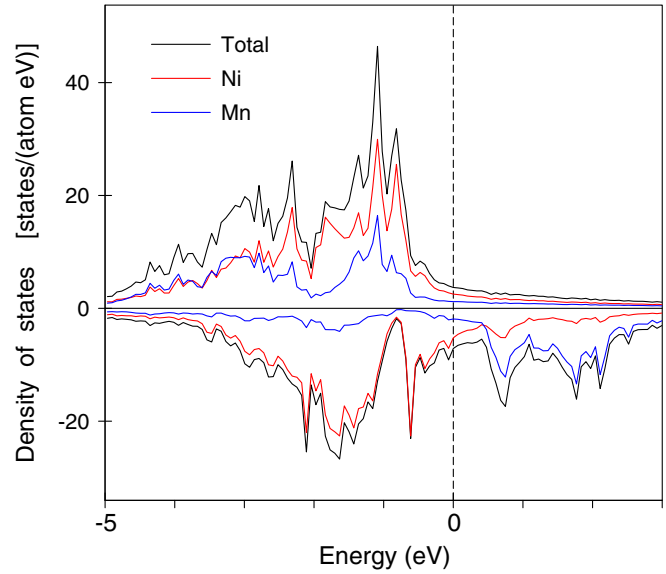


FIG. 7. Total and element-resolved spin-polarized density of states calculated for the $Ni_{53.2}Mn_{31.9}Sn_{15.6}$ Heusler alloy in the austenite phase. For clarity, the partial density of states for Sn, of an amplitude less than 0.5 states/(atom eV), is not shown.

Another reason for the low value of $R$ can be related to the proximity of $T_C$ to the measurement temperature $T_a$ and the possible reduction of the spin-flip probability parameter $a_{sf}$. The $R$ parameter is given by [23]

$$R = \frac{8 a_{sf} g_{el} k_B T_C^2 V_{at}}{(\mu_{at}/\mu_B) E_D^2}, \tag{10}$$

where $k_B$ is the Boltzmann constant, $V_{at}$ is the atomic volume, $\mu_{at}$ is the atomic magnetic moment, $\mu_B$ is the Bohr magneton, and $E_D = k_B \Theta_D$ is the Debye energy. For the $a_{sf}$ estimation, in Eq. (10) we used the obtained values for $R$ and $g_{el}$, and the Debye temperature $\Theta_D = 310$ K [81]. For the $\mu_{at}$ estimation, we assumed the *ab initio* calculated magnetic moment per atom, averaged over the unit cell, $\mu_{at} = 1.75\,\mu_B$. The obtained value of $a_{sf} = 0.09$ is about two times smaller as compared to Ni and close to that determined for Gd [23].

The eM3TM model was applied to explain the origin of the strong decrease of $H_k^{eff}$ with $F$ shown in Fig. 5(e). We have assumed that changes in the effective anisotropy field $H_k^{eff}$ with the fluence consist of changes in the sample magnetic anisotropy $H_k$ and shape anisotropy $4\pi M$, i.e., the equation $\Delta H_k^{eff}(F) = \Delta H_k(F) + 4\pi \Delta M(F)$ holds. The function $\Delta M(F)$ was obtained by performing a spatial and temporal double averaging procedure applied to the relative magnetization $m(t)$ solutions of Eqs. (9a)–(9d) as a function

of $F$. In the spatial averaging, it was taken into account that the fluence reaching different depths $z$ from the sample surface is diminished by a factor of $\exp(-z/d)$, where $d = \lambda/4\pi k$ is the light penetration depth equal to 20.5 nm for the extinction coefficient $k$ at the wavelength $\lambda = 800$ nm (see Sec. II). In the temporal averaging, the $m(t)$ solutions were averaged over the delay time $t$ up to two time constants $\tau$. As a result, we obtained the time and depth averaged relative demagnetization $\Delta m(F)$ function. The demagnetization function $\Delta M(F) = c\,\Delta m(F)$ was next fitted to the $\Delta H_k^{\mathrm{eff}}(F) = H_k^{\mathrm{eff}}(F) - H_k^{\mathrm{eff}}(F \to 0)$ [with $H_k^{\mathrm{eff}}(F)$ taken from Fig. 5(e) and $H_k^{\mathrm{eff}}(F \to 0) = 3.52$ kOe] with the use of a best matched scaling factor $c$. The obtained simulated function for $H_k^{\mathrm{eff}}(F)$ dependence in shown in Fig. 5(e) by the red triangles.

Three important conclusions can be drawn from the simulation performed. First, the eM3TM model very well reproduces the experimental dependence of the effective anisotropy field changes with the fluence. Second, $\Delta H_k^{\mathrm{eff}}(F)$ is fully determined by demagnetization $\Delta m(F)$, because the changes in the sample magnetic anisotropy are virtually zero [$\Delta H_k(F) = 0.020 \pm 0.035$ kOe]. Third, the eM3TM model adequately describes the critical slowing down effect of the demagnetization in the $T_C$ proximity for the $Ni_{54.3}Mn_{31.9}Sn_{13.8}$ Heusler-alloy film studied within the nanosecond time-delay long-range scale.

Analyzing $H_k^{\mathrm{eff}}$ vs $F$ in Fig. 5(e), one can draw the conclusion based on previous considerations that the $H_k^{\mathrm{eff}}(F)$ function inflection point at $F \approx 0.6$ mJ/cm$^2$ corresponds to nearly complete demagnetization at the sample surface. The laser pulse energy transfer to the deeper regions along the light penetration depth is reduced due to the absorption, hence the temperature stays below $T_C$ in these regions. This mechanism is responsible for the weaker $H_k^{\mathrm{eff}}(F)$ and $\Delta m(F)$ dependencies on $F$ in the range 0.6–0.9 mJ/cm$^2$.

Finally, it is worth commenting on the obtained result that the $H_k$ contribution to $H_k^{\mathrm{eff}}$ is negligible. This is because, in the $T_C$ vicinity, $H_k$ tends to zero faster than the magnetization itself (see, e.g., Ref. [84]).

In conclusion, in light of the results obtained, it can be stated that the slowing down of demagnetization observed is related to the low $R$ value in the Heusler alloy studied and caused by the proximity of $T_C$ to the measurement temperature. Similarly as in the case of Gd and oxide compounds, the low values of the $R$ parameter are mainly responsible for the relatively long demagnetization times in the ultrafast magnetization dynamics effects.

## IV. SUMMARY AND CONCLUSIONS

The time-resolved magneto-optical Kerr effect in the pump-probe measurement technique has been used to investigate ultrafast magnetization dynamics processes in an epitaxial $Ni_{54.3}Mn_{31.9}Sn_{13.8}$ Heusler-alloy film. Comprehensive studies of transient Kerr rotation were performed in a wide range of magnetic fields $H$ and pulse fluences $F$ as a function of delay time $t$ within a long-range, up to 3.5 ns, time window. In addition to the oscillatory spin precession component, in the measured signal, the slowly changing nonoscillating background, associated with critical slowing down demagnetization, was observed in both types of $H$- and $F$-dependent experimental scenarios. The separation of the components allowed us to estimate relatively high demagnetization times which are much larger than can be found for common ferromagnets. From the analysis of the oscillatory part, we determined the magnetization precession parameters—frequency $f$, relaxation time $\tau$, and amplitude $A$ as a function of $H$ and $F$. A uniform Kittel precession mode with a significant reduction of $f$ vs $F$ has been observed. The saturation effects of $A$ with both $H$ and $F$ were found. Based on the Landau-Lifshitz-Gilbert equation, the Gilbert damping parameter $\alpha$ and the effective magnetic anisotropy $H_k^{\mathrm{eff}}$ vs $H$ and $F$ were determined. A significant increase of $\alpha$ with $F$ has been found. The behavior of the precession amplitude versus $H$ and $F$ was explained in the frame of a phenomenological approach in which $A$ was assumed to depend on both $H_k^{\mathrm{eff}}$ and the difference of the equilibrium magnetization angles taken before and after pump-pulse excitation. It has been shown that the reduction of $A(F)$ for high fluences is a result of a significant $H_k^{\mathrm{eff}}(F)$ lowering which originates from the magnetization decrease due to the rise in the material temperature caused by temporary laser pulse heating. Good agreement of $A$ with the experiment was obtained for both measuring scenarios.

An extended microscopic three-temperature eM3TM model has been developed, in which an additional heat reservoir, representing the surroundings with a constant temperature $T_a$, was introduced. Within numerical solutions of the model we were able to precisely determine the nonoscillating signal background in the measured transient Kerr rotation dependencies. The obtained values of the demagnetization rate $R$ and electron-lattice coupling constant $g_{el}$, which were essential to explain the large slowing down effect of demagnetization in the $Ni_{54.3}Mn_{31.9}Sn_{13.8}$ alloy film, are of the order of the values observed for Gd, while they are more than an order of magnitude smaller than reported for Ni [23]. It has been found that the spin-flip probability $a_{sf}$ parameter is only about two times smaller than that reported for Ni [23]. It is shown that the main reason for the occurrence of long demagnetization times in the $Ni_{54.3}Mn_{31.9}Sn_{13.8}$ alloy film is the proximity of the $T_C$ temperature of the material. The numerical simulations performed in the frame of the extended eM3TM model reproduce the effective magnetic anisotropy field versus pump-pulse fluence, in excellent agreement with the experiment.

## ACKNOWLEDGMENTS

The authors would like to thank J. Dubowik for discussions. K.Z. acknowledges the financial support from the National Science Centre of Poland by the SONATA Project No. UMO-2016/23/D/ST3/02121.

[1] A. Barman and A. Haldar, in *Solid State Physics*, edited by R. E. Camley and R. L. Stamps (Academic, New York, 2014), Vol. 65, pp. 1–108.

[2] A. M. Kalashnikova, A. V. Kimel, and R. V. Pisarev, Phys.-Usp. **58**, 969 (2015).

[3] J. V. Bigot, W. Hübner, T. Rasing, and R. Chantrell, *Ultrafast Magnetism I* (Springer, Cham, 2015).

[4] K. Vahaplar, A. M. Kalashnikova, A. V. Kimel, D. Hinzke, U. Nowak, R. Chantrell, A. Tsukamoto, A. Itoh, A. Kirilyuk, and T. Rasing, Phys. Rev. Lett. **103**, 117201 (2009).

[5] J. Walowski and M. Münzenberg, J. Appl. Phys. **120**, 140901 (2016).

[6] Y. Xu, M. Deb, G. Malinowski, M. Hehn, W. Zhao, and S. Mangin, Adv. Mater. **29**, 1703474 (2017).

[7] M. L. M. Lalieu, R. Lavrijsen, and B. Koopmans, Nat. Commun. **10**, 110 (2019).

[8] A. Kirilyuk, A. V. Kimel, and T. Rasing, Rev. Mod. Phys. **82**, 2731 (2010).

[9] B. Jean-Yves and V. Mircea, Ann. Phys. **525**, 2 (2013).

[10] E. Beaurepaire, J.-C. Merle, A. Daunois, and J.-Y. Bigot, Phys. Rev. Lett. **76**, 4250 (1996).

[11] A. Mann, J. Walowski, M. Münzenberg, S. Maat, M. J. Carey, J. R. Childress, C. Mewes, D. Ebke, V. Drewello, G. Reiss, and A. Thomas, Phys. Rev. X **2**, 041008 (2012).

[12] W. He, B. Hu, Q.-F. Zhan, X.-Q. Zhang, and Z.-H. Cheng, Appl. Phys. Lett. **104**, 142405 (2014).

[13] S. Pan, T. Seki, K. Takanashi, and A. Barman, Phys. Rev. Appl. **7**, 064012 (2017).

[14] L. A. Shelukhin, V. V. Pavlov, P. A. Usachev, P. Y. Shamray, R. V. Pisarev, and A. M. Kalashnikova, Phys. Rev. B **97**, 014422 (2018).

[15] W. Li, J. Yan, M. Tang, S. Lou, Z. Zhang, X. L. Zhang, and Q. Y. Jin, Phys. Rev. B **97**, 184432 (2018).

[16] S. Mondal and A. Barman, Phys. Rev. Appl. **10**, 054037 (2018).

[17] J. Güdde, U. Conrad, V. Jähnke, J. Hohlfeld, and E. Matthias, Phys. Rev. B **59**, R6608(R) (1999).

[18] E. Carpene, E. Mancini, C. Dallera, M. Brenna, E. Puppin, and S. De Silvestri, Phys. Rev. B **78**, 174422 (2008).

[19] T. Kampfrath, R. G. Ulbrich, F. Leuenberger, M. Münzenberg, B. Sass, and W. Felsch, Phys. Rev. B **65**, 104429 (2002).

[20] T. Kise, T. Ogasawara, M. Ashida, Y. Tomioka, Y. Tokura, and M. Kuwata-Gonokami, Phys. Rev. Lett. **85**, 1986 (2000).

[21] Q. Zhang, A. V. Nurmikko, G. X. Miao, G. Xiao, and A. Gupta, Phys. Rev. B **74**, 064414 (2006).

[22] G. M. Muller, J. Walowski, M. Djordjevic, G.-X. Miao, A. Gupta, A. V. Ramos, K. Gehrke, V. Moshnyaga, K. Samwer, J. Schmalhorst, A. Thomas, A. Hutten, G. Reiss, J. S. Moodera, and M. Munzenberg, Nat. Mater. **8**, 56 (2009).

[23] B. Koopmans, G. Malinowski, F. Dalla Longa, D. Steiauf, M. Fahnle, T. Roth, M. Cinchetti, and M. Aeschlimann, Nat. Mater. **9**, 259 (2010).

[24] J.-Y. Bigot, M. Vomir, L. Andrade, and E. Beaurepaire, Chem. Phys. **318**, 137 (2005).

[25] S. Mizukami, F. Wu, A. Sakuma, J. Walowski, D. Watanabe, T. Kubota, X. Zhang, H. Naganuma, M. Oogane, Y. Ando, and T. Miyazaki, Phys. Rev. Lett. **106**, 117201 (2011).

[26] Y. Liu, L. R. Shelford, V. V. Kruglyak, R. J. Hicken, Y. Sakuraba, M. Oogane, and Y. Ando, Phys. Rev. B **81**, 094402 (2010).

[27] D. Steil, O. Schmitt, R. Fetzer, T. Kubota, H. Naganuma, M. Oogane, Y. Ando, A. K. Suszka, O. Idigoras, G. Wolf, B. Hillebrands, A. Berger, M. Aeschlimann, and M. Cinchetti, New J. Phys. **16**, 063068 (2014).

[28] Y. K. Takahashi, Y. Miura, R. Choi, T. Ohkubo, Z. C. Wen, K. Ishioka, R. Mandal, R. Medapalli, H. Sukegawa, S. Mitani, E. E. Fullerton, and K. Hono, Appl. Phys. Lett. **110**, 252409 (2017).

[29] F. Hoveyda, E. Hohenstein, R. Judge, and S. Smadici, J. Phys.: Condens. Matter **30**, 195802 (2018).

[30] M. Sultan, U. Atxitia, A. Melnikov, O. Chubykalo-Fesenko, and U. Bovensiepen, Phys. Rev. B **85**, 184407 (2012).

[31] M. Djordjevic and M. Münzenberg, Phys. Rev. B **75**, 012404 (2007).

[32] T. Roth, A. J. Schellekens, S. Alebrand, O. Schmitt, D. Steil, B. Koopmans, M. Cinchetti, and M. Aeschlimann, Phys. Rev. X **2**, 021006 (2012).

[33] T. Ogasawara, K. Ohgushi, Y. Tomioka, K. S. Takahashi, H. Okamoto, M. Kawasaki, and Y. Tokura, Phys. Rev. Lett. **94**, 087202 (2005).

[34] B. Liu, W. Niu, Y. Chen, X. Ruan, Z. Tang, X. Wang, W. Liu, L. He, Y. Li, J. Wu, S. Tang, J. Du, R. Zhang, and Y. Xu, Adv. Mater. **31**, 1806443 (2019).

[35] H. J. Mohamad, L. R. Shelford, M. Aziz, U. A. S. Al-Jarah, R. Al-Saigh, R. A. J. Valkass, S. Marmion, B. J. Hickey, and R. J. Hicken, Phys. Rev. B **96**, 134431 (2017).

[36] T. P. Ma, S. F. Zhang, Y. Yang, Z. H. Chen, H. B. Zhao, and Y. Z. Wu, J. Appl. Phys. **117**, 013903 (2015).

[37] J. Walowski, M. D. Kaufmann, B. Lenk, C. Hamann, J. McCord, and M. Münzenberg, J. Phys. D: Appl. Phys. **41**, 164016 (2008).

[38] S. Azzawi, A. T. Hindmarch, and D. Atkinson, J. Phys. D: Appl. Phys. **50**, 473001 (2017).

[39] C. Papusoi, T. Le, C. C. H. Lo, C. Kaiser, M. Desai, and R. Acharya, J. Phys. D: Appl. Phys. **51**, 325002 (2018).

[40] S. Qiao, S. Nie, J. Zhao, and X. Zhang, Appl. Phys. Lett. **105**, 172406 (2014).

[41] S. Qiao, S. Nie, J. Zhao, Y. Huo, Y. Wu, and X. Zhang, Appl. Phys. Lett. **103**, 152402 (2013).

[42] B. Liu, X. Ruan, Z. Wu, H. Tu, J. Du, J. Wu, X. Lu, L. He, R. Zhang, and Y. Xu, Appl. Phys. Lett. **109**, 042401 (2016).

[43] Y. Liu, L. R. Shelford, V. V. Kruglyak, R. J. Hicken, Y. Sakuraba, M. Oogane, Y. Ando, and T. Miyazaki, J. Appl. Phys. **101**, 09C106 (2007).

[44] S. Pan, S. Mondal, T. Seki, K. Takanashi, and A. Barman, Phys. Rev. B **94**, 184417 (2016).

[45] T. Krenke, E. Duman, M. Acet, E. F. Wassermann, X. Moya, L. Manosa, and A. Planes, Nat. Mater. **4**, 450 (2005).

[46] S. Chatterjee, S. Giri, S. Majumdar, and S. K. De, J. Phys. D: Appl. Phys. **42**, 065001 (2009).

[47] M. Khan, A. K. Pathak, M. R. Paudel, I. Dubenko, S. Stadler, and N. Ali, J. Magn. Magn. Mater. **320**, L21 (2008).

[48] H. E. Karaca, I. Karaman, B. Basaran, Y. Ren, Y. I. Chumlyakov, and H. J. Maier, Adv. Funct. Mater. **19**, 983 (2009).

[49] V. Antonov, L. Bekenov, S. Uba, A. Bonda, and L. Uba, J. Alloys Compd. **695**, 1826 (2017).

[50] Y. Ma, S. Awaji, M. Watanabe, M. Matsumoto, and N. Kobayashi, Solid State Commun. **113**, 671 (2000).

[51] M. Zhang, G. Cao, H. Tian, S. Sun, Z. Li, X. Li, C. Guo, Z. Li, H. Yang, and J. Li, Phys. Rev. B **96**, 174203 (2017).

[52] M. Zhang, Z.-A. Li, H. Tian, H. Yang, and J. Li, Appl. Phys. Lett. **113**, 133103 (2018).

[53] S. O. Mariager, C. Dornes, J. A. Johnson, A. Ferrer, S. Grübel, T. Huber, A. Caviezel, S. L. Johnson, T. Eichhorn, G. Jakob, H. J. Elmers, P. Beaud, C. Quitmann, and G. Ingold, Phys. Rev. B **90**, 161103(R) (2014).

[54] G. Lantz, M. J. Neugebauer, M. Kubli, M. Savoini, E. Abreu, K. Tasca, C. Dornes, V. Esposito, J. Rittmann, Y. W. Windsor, P. Beaud, G. Ingold, and S. L. Johnson, Phys. Rev. Lett. **119**, 227207 (2017).

[55] A. Bonda, S. Uba, K. Załęski, J. Dubowik, and L. Uba, Acta Phys. Pol., A **133**, 501 (2018).

[56] J. Dubowik, K. Załęski, I. Gościańska, H. Głowiński, and A. Ehresmann, Appl. Phys. Lett. **100**, 162403 (2012).

[57] J. Dubowik, I. Gościańska, K. Załęski, H. Głowiński, A. Ehresmann, G. Kakazei, and S. A. Bunyaev, Acta Phys. Pol., A **121**, 1121 (2012).

[58] F. Dalla Longa, J. T. Kohlhepp, W. J. M. de Jonge, and B. Koopmans, Phys. Rev. B **75**, 224431 (2007).

[59] R. Wilks, R. J. Hicken, M. Ali, B. J. Hickey, J. D. R. Buchanan, A. T. G. Pym, and B. K. Tanner, J. Appl. Phys. **95**, 7441 (2004).

[60] R. Wilks, N. D. Hughes, and R. J. Hicken, J. Phys.: Condens. Matter **15**, 5129 (2003).

[61] A. Bonda, S. Uba, and L. Uba, Acta Phys. Pol., A **121**, 1225 (2012).

[62] A. N. Yaresko, L. Uba, S. Uba, A. Y. Perlov, R. Gontarz, and V. N. Antonov, Phys. Rev. B **58**, 7648 (1998).

[63] J. Miltat, G. Albuquerque, and A. Thiaville, An introduction to micromagnetics in the dynamic regime, in *Spin Dynamics in Confined Magnetic Structures I*, edited by B. Hillebrands and K. Ounadjela (Springer, Berlin, 2002), pp. 1–33.

[64] H. Kronmüller, General micromagnetic theory, in *Handbook of Magnetism and Advanced Magnetic Materials* (Wiley, New York, 2007).

[65] D. Kumar and A. O. Adeyeye, J. Phys. D: Appl. Phys. **50**, 343001 (2017).

[66] S. Mizukami, Y. Ando, and T. Miyazaki, Jpn. J. Appl. Phys. **40**, 580 (2001).

[67] D. Talbayev, H. Zhao, G. Lüpke, A. Venimadhav, and Q. Li, Phys. Rev. B **73**, 014417 (2006).

[68] H. B. Zhao, D. Talbayev, Q. G. Yang, G. Lüpke, A. T. Hanbicki, C. H. Li, O. M. J. van 't Erve, G. Kioseoglou, and B. T. Jonker, Appl. Phys. Lett. **86**, 152512 (2005).

[69] S. Tomimoto, M. Matsubara, T. Ogasawara, H. Okamoto, T. Kimura, and Y. Tokura, Phys. Rev. Lett. **98**, 017402 (2007).

[70] S. Mizukami, A. Sakuma, T. Kubota, Y. Kondo, A. Sugihara, and T. Miyazaki, Appl. Phys. Lett. **103**, 142405 (2013).

[71] L. Uba, A. Bonda, S. Uba, L. V. Bekenov, and V. N. Antonov, J. Phys.: Condens. Matter **29**, 275801 (2017).

[72] H. Q. Tu, B. Liu, D. W. Huang, X. Z. Ruan, B. You, Z. C. Huang, Y. Zhai, Y. Gao, J. Wang, L. J. Wei, Y. Yuan, Y. B. Xu, and J. Du, Sci. Rep. **7**, 43971 (2017).

[73] K. Dadda, S. Alleg, S. Souilah, J. Suňol, E. Dhahri, L. Bessais, and E. Hlil, J. Alloys Compd. **735**, 1662 (2018).

[74] P. Zhang, T. L. Phan, N. H. Duc, N. H. Dan, and S. C. Yu, IEEE Trans. Magn. **48**, 3753 (2012).

[75] V. N. Kats, T. L. Linnik, A. S. Salasyuk, A. W. Rushforth, M. Wang, P. Wadley, A. V. Akimov, S. A. Cavill, V. Holy, A. M. Kalashnikova, and A. V. Scherbakov, Phys. Rev. B **93**, 214422 (2016).

[76] M. van Kampen, C. Jozsa, J. T. Kohlhepp, P. LeClair, L. Lagae, W. J. M. de Jonge, and B. Koopmans, Phys. Rev. Lett. **88**, 227201 (2002).

[77] A. A. Rzhevsky, B. B. Krichevtsov, D. E. Bürgler, and C. M. Schneider, Phys. Rev. B **75**, 224434 (2007).

[78] I. Petrila and V. Manta, Comput. Phys. Commun. **185**, 2874 (2014).

[79] I. Petrila, F. Ungureanu, and V. Manta, J. Comput. Electron. **14**, 627 (2015).

[80] N. Bergeard, M. Hehn, S. Mangin, G. Lengaigne, F. Montaigne, M. L. M. Lalieu, B. Koopmans, and G. Malinowski, Phys. Rev. Lett. **117**, 147203 (2016).

[81] V. A. Chernenko, J. M. Barandiarán, J. R. Fernández, D. P. Rojas, J. Gutiérrez, P. Lázpita, and I. Orue, J. Magn. Magn. Mater. **324**, 3519 (2012).

[82] V. K. Sharma, M. K. Chattopadhyay, R. Kumar, T. Ganguli, P. Tiwari, and S. B. Roy, J. Phys.: Condens. Matter **19**, 496207 (2007).

[83] J. Kimling, J. Kimling, R. B. Wilson, B. Hebler, M. Albrecht, and D. G. Cahill, Phys. Rev. B **90**, 224408 (2014).

[84] J. B. Staunton, L. Szunyogh, A. Buruzs, B. L. Gyorffy, S. Ostanin, and L. Udvardi, Phys. Rev. B **74**, 144411 (2006).